## Viscosity and Crystal Morphology Data of Anorthite Bearing

# **2 Synthetic Coal Slag Systems**

- 3 Jan Peter Schupsky\*a, Olga Saara, Guixuan Wua,b, Matthias Dohrnc, Michael Müllera
- 4 a Institute of Energy and Climate Research (IEK-2), Forschungszentrum Jülich GmbH,
- 5 52425 Jülich, Germany
- 6 <sup>b</sup> GTT Technologies, 52134 Herzogenrath, Germany
- 7 ° RWE Power AG, Werkstraße, 50129 Bergheim, Germany

8

9

1

#### **Abstract**

10 In this study, three synthetic SiO<sub>2</sub>-Al<sub>2</sub>O<sub>3</sub>-CaO-Fe<sub>2</sub>O<sub>3</sub>(-MgO) coal slag systems (ST-D-11 2, HKT, SOM-1) with varying basicity were investigated on their viscosity and the 12 dominant crystallisation product: anorthite (CaAl<sub>2</sub>Si<sub>2</sub>O<sub>8</sub>). To predict crystallisation 13 products, thermodynamic equilibrium calculations were executed using FactSage and 14 the GTox database. Anorthite is predicted as a major crystallising phase in the slags. 15 High temperature viscosimetry revealed non-Newtonian behaviour of the slags below 16 1275 °C. Additional viscosity measurements revealed viscosity deviations, based on 17 crystallisation. Post-experimental analysis of the slags revealed the presence of 18 elongated crystals with anorthite composition. Additional quenching experiments were 19 performed and crystallisation results of the HKT slag were exemplarily shown in this 20 study. Quenched samples were analysed by XRD and SEM-EDX to determine the 21 crystallised phases and the crystal structure. Anorthite was identified as the dominant 22 phase in the HKT slag but also in the ST-D-2 and SOM-1 slag system. As 23 crystallisation strongly influences slag viscosity, a phase analysis of anorthite was 24 conducted. The crystal morphology of anorthite displayed a common elongated 25 characteristic and was generalised as a tetragonal prism with variations in its 26 dimensions. Crystal size measurements ascertained constant small crystal sizes at 27 temperatures below 1100 °C, and exhibited an increase of anorthite length with increasing temperatures above 1100 °C. Additionally, the aspect ratio was examined 28 29 to ensure a complete three-dimensional characterisation of the anorthite phase. Crystal 30 morphology data can be used in a future viscosity model as enhancing parameters to 31 enable the calculation of viscosities for partly crystallised slags.

- Keywords: Entrained flow gasification; coal slag; slag viscosity, crystallisation;
- anorthite; crystal morphology

34

35

32

# 1 Introduction

36	In past decades, IGCC has been applied to conventional coal conversion facilities such
37	as entrained-flow gasifiers to improve the efficiency and to reduce the CO <sub>2</sub> emissions
38	[1]. Gasifiers partly produce slag as side product from inorganic compounds during
39	operation. In contrast, the organic releases are accountable for the production of
40	syngas (e.g. CO, H <sub>2</sub> ), which can be used as a resource for chemical and pharma
41	industries [2, 3].
42	Throughout the entrained flow gasifier operation at temperatures between 1200 °C and
43	1700 °C, a thin layer of slag is produced protecting the refractory walls from corrosion
44	and alteration [3-6]. A maximum viscosity of 25 Pa·s guarantees a smooth and
45	sufficient slag flow [7]. However, the viscosity of slag, and therefore its flow
46	behaviour, is primarily influenced by the temperature and secondly by the appearance
47	of crystallisation in the liquid slag [8-10]. The crystallisation in liquid slag can lead to
48	a significant increase of the viscosity, as described in the model of relative viscosity
49	by Seebold, Wu and Müller [3] and may further lead to a blockage of slag tapping.
50	In the field of magmatic liquids in the 1970s, Shaw [11] and Urbain et al. [12]
51	developed models that incorporated the influence of slag chemistry on viscosity. In the
52	past decades, those models have been improved and new models have been postulated,
53	such as the Kondratiev-Jak-model [13] or the Avramov model [14]. Recent works by
54	Wu et al. [2, 15] describe a structural based model that proved its applicability for
55	multicomponent systems. As the viscosity of partially crystallised slags is not only
56	related to the viscosity of pure liquid slags, parameters such as volume fraction of
57	crystals, crystal size, distribution of crystal size, crystal morphology, and shear rate
58	generate a high degree of complexity.
59	The crystallisation behaviour of slags was investigated in several recent studies [3, 16-
60	21]. Some studies provide meaningful contributions as the crystallisation is associated

with a significant slag viscosity increase, due to its rheological influence [3, 22]. Other studies highly focus on crystallisation kinetics, but do not investigate crystal phase mineralogy or morphology [17, 20, 23]. A commonly used method to describe slag crystallisation is the single hot thermocouple technique (SHTT) [20, 24, 25]. SHTT serves a high resolution on crystallisation kinetics. However, crystallographic and chemical properties of the crystallised phases are not determined. In a recent study, the crystallised phases of a synthetic lignite slag were investigated [26]. A brief literature review of coal slags summarised that only few crystallised phases need to be investigated, which cover all relevant crystallised phases [26]. Olivine and melilite were quantified on their crystal morphology and potential viscosity model requirements were described [26]. This study aims to follow this approach and provides additional crystal morphology data for another relevant crystal phase anorthite. This study analyses the crystallisation processes of three synthetically produced SiO<sub>2</sub>-Al<sub>2</sub>O<sub>3</sub>-CaO-Fe<sub>2</sub>O<sub>3</sub>(-MgO) slag systems under reduced gasifier conditions. The analysed slag systems partly refer to a real coal ashes named HKT and ST-D-2 [27, 28] Real HKT and ST-D-2 slag were investigated in a previous work [3], though without the focus set on the crystallised anorthite phase. This study aims to analyse the crystallised phases of synthetic HKT, ST-D-2 and SOM-1 slag with special focus on the dominant anorthite phase. In the end, crystal morphology data of anorthite will be provided that can be used in addition to already published melilite and olivine morphology data as enhancing parameters for a viscosity model for partly crystallised slags [26]. An initial characterisation of the slags was performed by equilibrium calculations. The slags' viscosities were determined by viscosity measurements. To investigate slag crystallisation characteristics, quenching experiments were performed. The samples were investigated isothermally to keep time as the only variable. The postexperimental sample analysis was performed by microscopy, XRD, and SEM-EDX. Time-temperature-transformation (TTT) diagrams were generated to ascertain

61

62

63

64

65

66

67

68

69

70

71

72

73

74

75

76

77

78

79

80

81

82

83

84

85

86

87

88

89

incubation times for crystallisation. Lastly, anorthite was identified as the dominant phase in all slag systems and a generalised morphology was defined. Based on the defined morphology, anorthite crystals were quantified on their crystal length and crystal aspect ratio (length/width), resulting in a morphology dataset for future viscosity model for partial crystallised slags.

95

96

97

98

99

100

101

102

103

104

105

106

107

108

109

110

111

112

113

114

115

90

91

92

93

94

# 2 Experimental

#### 2.1 Synthetic slag samples

The investigated synthetic HKT and ST-D-2 slag systems are based on real lignite and hard coal slags, investigated in a previous study [3] and therefore chosen. To further determine the influence of the slag composition and basicity on the crystallisation results, a third slag system was created that has an ongoing higher basicity, due to lower fractions of SiO<sub>2</sub> (Table 1). Accordingly, the three slag systems cover a bandwidth of typical slag compositions and therefore results are seen as broadly applicable. To achieve constant slag chemistry and to improve comparability of experimental results, not the original slags were used but respective slags were produced synthetically [29, 30]. The slag compositions consist of four, respectively five oxides SiO<sub>2</sub>, Al<sub>2</sub>O<sub>3</sub>, CaO, Fe<sub>2</sub>O<sub>3</sub> and MgO [28]. Highly reactive and volatile alkali-oxides were excluded due to the aforementioned reasons. The synthetic slag samples were produced on the basis of different oxides with high purity (Alfa Aesar, Massachusetts, U.S. and Merck, Darmstadt, Germany). Initially, the five analytical reagents were balanced, mixed together, and dried subsequently at 100 °C for 10 h. Afterwards, the dried powder was blended for 24 h to ensure complete homogenisation. Finally, the chemical composition of the synthetic slags was verified using ICP-OES.

Table 1: Composition of the investigated synthetic slag systems, analysed with ICP-OES.

		SiO <sub>2</sub>	Al <sub>2</sub> O <sub>3</sub>	CaO	Fe <sub>2</sub> O <sub>3</sub>	MgO	Basicity
ST-D-2	wt%	60.9	21.6	10.6	6.9	-	0.12
HKT	wt%	54.7	22.3	14.6	2.6	5.8	0.26
SOM-1	wt%	47.6	19.2	14.4	9.2	9.6	0.32

### 2.2 Thermodynamic equilibrium calculations

Thermochemical calculations via FactSage computational package (GTT Technologies, Herzogenrath, Germany) are a method commonly used to examine crystallised phases in oxidic slag systems [3, 16, 31, 32]. The Equilib module of FactSage can predict equilibrium conditions of all involved potential phases by using Gibbs free energy minimisation in conjunction with oxide databases. In this study, calculations were executed using software version 6.4. The GTox database was used for the calculations [33]. Equilibrium calculations were executed in the range between 900 °C and 1400 °C with a 10 °C interval. To represent gasifier conditions, calculations were performed with a oxygen partial pressure of 10<sup>-12</sup> bar. FactSage results were used as a reference to compare thermodynamically crystallised phases with the phases determined throughout the quenching experiment.

## 2.3 High temperature viscosimetry

The viscosity of slags was analysed using a high temperature rotational viscometer. Same device was used in the previous study [3] and provided reliable results. A rheometer type RC1 (RheoTec Meßtechnik GmbH, Ottendorf-Okrilla, Germany) was used in combination with a high temperature furnace that was located below the rheometer. It can be operated applying a defined shear rate as well as applying a fixed torque [34]. The maximum torque is stated as 50 mN·m (milli newtonmeter) and the maximum rotation per minute as 800 rpm [34]. However, for the performed experiments the maximum parameters were set to 40 mN·m and 400 rpm respectively, to create analogue parameters with the recent study of Seebold [3].

Slag samples were investigated isothermally in a stepwise manner. Subsequently after the maximum temperature of 1500 °C was reached, the furnace cooled down and started the measurements at 1425 °C. The rheometer measured the required torque, regarding to the applied rotation in steps of 25 °C. Additionally, isothermal measurements with 7 hours of holding time were performed at lower temperatures to document the incubation time of crystallisation as well as their impact on the slag

viscosity. Additionally, the stirred samples were analysed after the experiment via microscopy and SEM-EDX to identify the crystallised phases.

To ensure the trustworthiness of the experimental set up and to exclude methodological faults, a comparison of the viscosity data with viscosity calculations was made. Thus, the viscosity values for the analysed slag systems were determined, applying the latest version of the viscosity model of Wu [2, 15, 35]. The model enables the viscosity calculation of multicomponent systems, including  $Fe_2O_3$ . Self-evidently, only Newtonian behaviour can be modelled and a possible impact of crystals cannot be predicted.

155

156

157

158

159

160

161

162

163

164

165

166

167

168

169

170

171

172

173

174

175

146

147

148

149

150

151

152

153

154

#### 2.4 Quenching Experiment

To examine the crystallisation characteristics of the synthetic SiO<sub>2</sub>-Al<sub>2</sub>O<sub>3</sub>-CaO-MgO-Fe<sub>2</sub>O<sub>3</sub> slag system, quenching experiments were conducted. Firstly, an amount of approximately 1-1.2 g of slag powder was filled in each molybdenum crucible. The cylindrical Mo-crucibles are 33 mm in height and 10 mm in diameter. In contrast to other crucible materials such as Al<sub>2</sub>O<sub>3</sub>, molybdenum was chosen due to a lack of interactions with oxidic melts [36]. To ensure sample homogeneity, the filled crucibles were heat-treated in a high temperature furnace (HTF 18/8, Carbolite Gero GmbH & Co. KG, Neuhausen, Germany). The samples experienced a maximum temperature of 1550 °C with a holding time of 5 h to ensure complete melting of the oxide powder. To prevent oxidation of the Mo-crucibles, a reducing Ar/4%H<sub>2</sub>-atmopshere was applied during the treatment [36]. After the pre-treatment, crucibles were placed in the Al<sub>2</sub>O<sub>3</sub> vertical tube of the quenching furnace (Fig. 1). A special sample holder was designed that carries up to five crucibles in the vertical furnace at the same time. This sample holder also serves the possibility to quench the crucibles successively. The bottom part of the vertical Al<sub>2</sub>O<sub>3</sub> tube was submerged in a water basin. In other studies [21, 37], furnaces are sealed via flanges to ensure constant atmosphere above the quenching unit. As these flanges are opened for the quenching procedure, air is flooding the furnace and the atmosphere is not constant any longer. In contrast, the aforementioned set up used in

this study guarantees a constant atmosphere. Thus, contact with higher oxygen partial pressures was precluded during the whole procedure. Reducing conditions were achieved by flushing the corundum tube with 150 ml/min of Ar/4%H<sub>2</sub>-gas through the submerged tube orifice (Fig. 1). The absence of MoO<sub>x</sub> phases on the crucible surfaces confirms partial pressures of less than  $P(O_2) = 10^{-12}$  bar [38]. The tube upper orifice was covered with a custom designed Al<sub>2</sub>O<sub>3</sub>-foam plate. This set up was already used in a previous study for slag investigations [26].

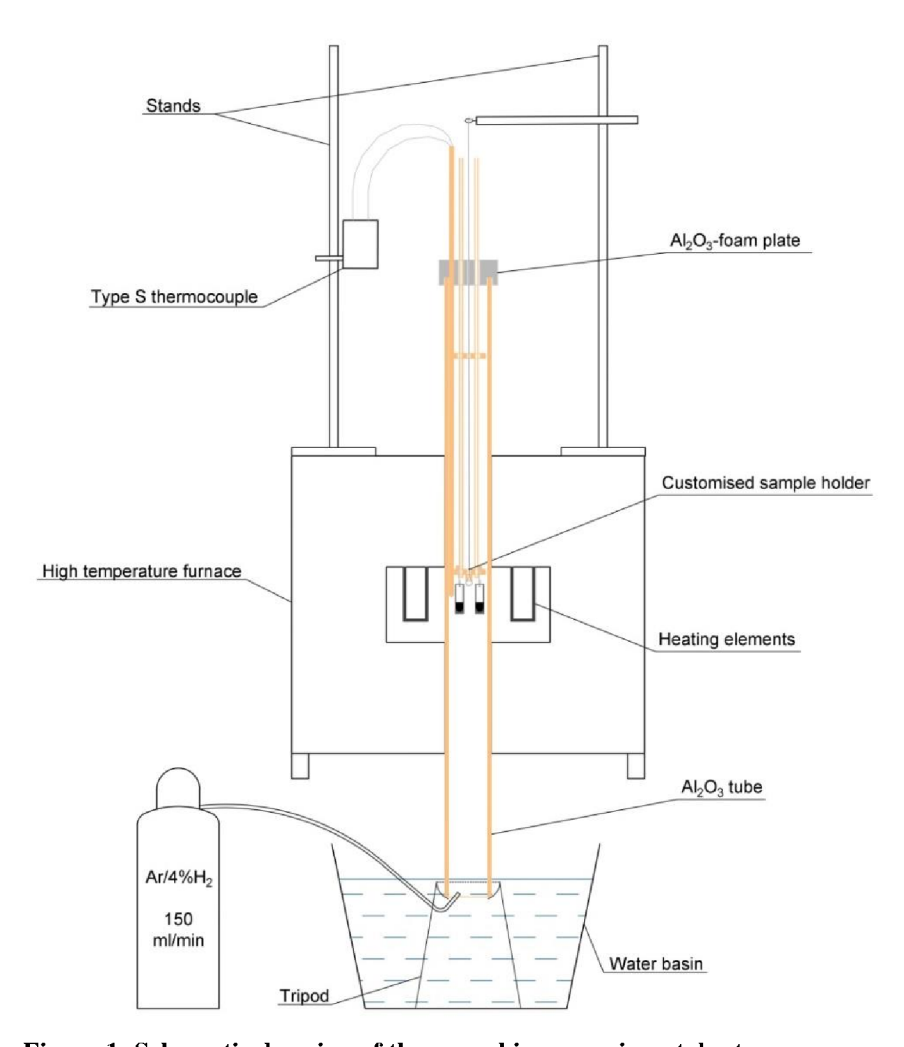


Figure 1: Schematic drawing of the quenching experimental set up.

The crystallisation processes under supercooling conditions were investigated by selecting ten isothermal temperature profiles (Fig. 2). Firstly, the preheated samples were heated to 1450 °C and held for 1 h to generate a homogeneous melt. Afterwards, samples were cooled down with a rate of -7 K/min to the individual isothermal sections. The whole investigations cover a temperature range between 850 and

1300 °C. To provide high sample resolution, profiles were set in 50 °C steps (Fig. 2). After reaching a certain isothermal step, samples were quenched time-dependently after 0, 1, 4, 7 and occasionally 24 hours of holding time, respectively. This approach facilitated the examination of crystal evolution over time, including the kinetic influence on crystal growth. The 24 h holding-time-span was chosen to represent conditions close to the equilibrium state. Hereafter, samples were prepared for analysis, starting with slicing the crucibles into two hemispheres and embedding them into epoxy resin. Afterwards, crucibles were ground and polished to enable a 2-dimensional analysis of the slag sample by XRD and SEM-EDX. Additionally, some of the quenched samples were separated from their crucibles and ground to perform XRD analysis of sample powder.

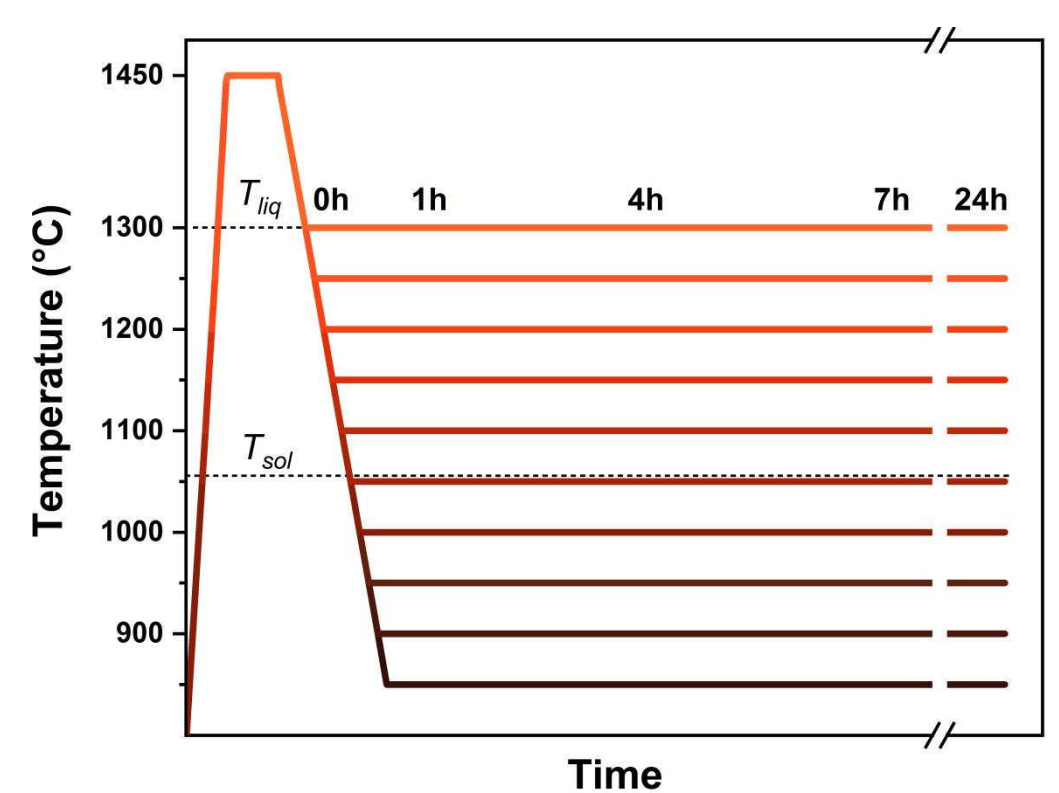


Figure 2: Temperature profiles applied in the quenching experiments.

2.5 Post-experimental analysis

First investigations on the slag structure were performed using a KEYENCE VHX-S550E digital microscope (KEYENCE DEUTSCHLAND GmbH, Neu-Isenburg, Germany). High resolution images with magnifications up to a factor of 200 have been shot under ring light (deep vision) and coaxial light (surface topology). Completely

208 amorphous samples were identified and distinguished from crystallised samples. 209 Crystallised samples were subsequently analysed by XRD and SEM. 210 To determine the crystallised phases, XRD measurements of several representative samples have been conducted. Firstly, the cross sections of embedded samples were 211 212 analysed to compare crystal orientation with detected hkl (i.e. miller indices). 213 Secondly, slag samples were ground into powders before the XRD analysis to enhance 214 signal quality. A Panalytical EMPYREAN (Malvern Panalytical, Almelo, 215 Netherlands) device was utilized for the μ-XRD sample analysis. A Cu Kα anode (40 216 kV and 40 mA) was installed during the measurements. Datasets from the ICSD 217 (Inorganic Crystal Structure Database, FIZ Karlsruhe, Germany) database have been 218 chosen for the comparison with experimental results. 219 Further sample investigations have been performed by SEM and SEM-EDX analysis. 220 Measurements were carried out by Zeiss Merlin II and Supra 50 VP (Carl Zeiss 221 Microscopy GmbH, Jena, Germany) devices. The samples were prepared, applying an 222 Ir-sputter coating, beforehand. In this manner, the vast majority of all crystallised 223 samples were examined. In addition to taking high resolution images of crystallised 224 phases, single EDX measurements as well as EDX element mappings were performed 225 to gather chemical information. Based on the SEM images, the crystal analysis was 226 applied on the anorthite phase. The length and width of individual anorthite crystals

3 Results and discussion

227

228

229

230

231

232

233

234

235

236

#### 3.1 Equilibrium calculations

FactSage Equilib calculations reveal that anorthite ( $CaAl_2Si_2O_8$ ) is the first phase to crystallise in all slag systems. Also, anorthite seemingly forms the highest fraction of all crystallised phases in the three slag systems. With an increase of the slags basicity, the liquidus temperature declines from 1320 °C (ST-D-2) to 1250 °C (SOM-1) slag. In the ST-D-2 slag, cristobalite ( $SiO_2$ ) is the second phase to crystallise, followed by minor fractions of cordierite ( $Mg_2Al_4Si_5O_{18}$ ) and lastly olivine ((Ca,Fe)<sub>2</sub> $SiO_4$ ) (Fig. 3).

were measured and its aspect ratio (length/width) was calculated (chapter 3.5).

In the HKT slag, anorthite content increases to approximately 47 wt% at 1050 °C. At temperatures of 1260 °C and 1250 °C cordierite and cristobalite begin to form, respectively. Their fractions increase almost constantly and reach a maximum of about 13 to 14 wt%. Clinopyroxene (AB(Si,Al)<sub>2</sub>O<sub>6</sub>) (A = Ca, Mg, Fe<sup>2+</sup>, B = Ca, Mg, Fe<sup>2+</sup>, Fe<sup>3+</sup>) is the fourth predicted phase to crystallise (Fig. 3). In the SOM-1 slag system, anorthite is accompanied by cordierite at 1150 °C. Clinopyroxene and olivine are additional phases that are expected to grow at lower temperatures of approx. 1100 °C. It can be summarised that anorthite is the dominant phase in all slag systems, enabling a suitable investigation of the anorthite phase.

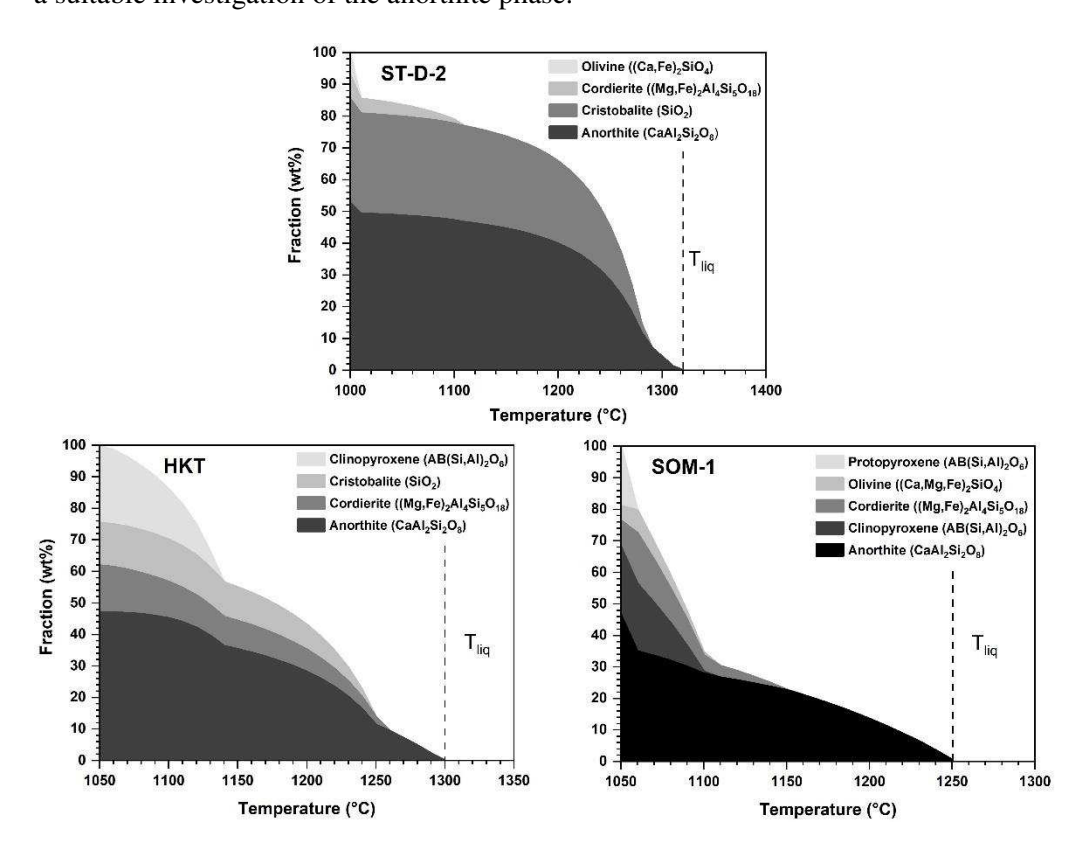


Figure 3: FactSage Equilib prediction of phase formation of the synthetic ST-D-2, HKT and SOM-1 slag system under  $p(O_2) = 10^{-12}$ .

#### 3.2 Viscosity measurements

The comparison of the experimental data with the modelling results reveals an overall satisfactory agreement (Fig. 4). ST-D-2 slag data align very well with the modelling results. At temperatures below 1350 °C, a tendency of relatively higher viscosities can be identified. For 1250 °C and 1275 °C it can be vaguely argued that the present

discrepancy between experimental and calculation results could be based on non-Newtonian behaviour of the ST-D-2 slag during measurements.

The gathered HKT viscosity data are also reasonable, as the comparison with the theoretical modelling results prove (Fig. 4). Yet, the accordance accounts only for temperatures above 1275 °C. The drastic viscosity increase at 1275 °C and 1250 °C is clearly not covered by the modelling results. If crystallisation accounted for this phenomenon, the subsequently following isothermal viscosity measurement will uncover the potential presence of crystals in the HKT slag.

The SOM-1 slag displays a generally higher viscosity in relation to the calculated viscosity values (Fig. 4). The measured values exceed relative constantly the model results by approx. 15 Pa·s. By also focussing on the distinct viscosity increase at 1225 °C, the comparison indicates that non-Newtonian behaviour of SOM-1 slag was also present during the measurements (Fig. 4). It can be summarised that HKT and SOM-1 slag displayed non-Newtonian behaviour below 1300 °C and 1250 °C, which is in very good agreement with the liquidus temperatures predicted by the FactSage calculations (Fig. 3).

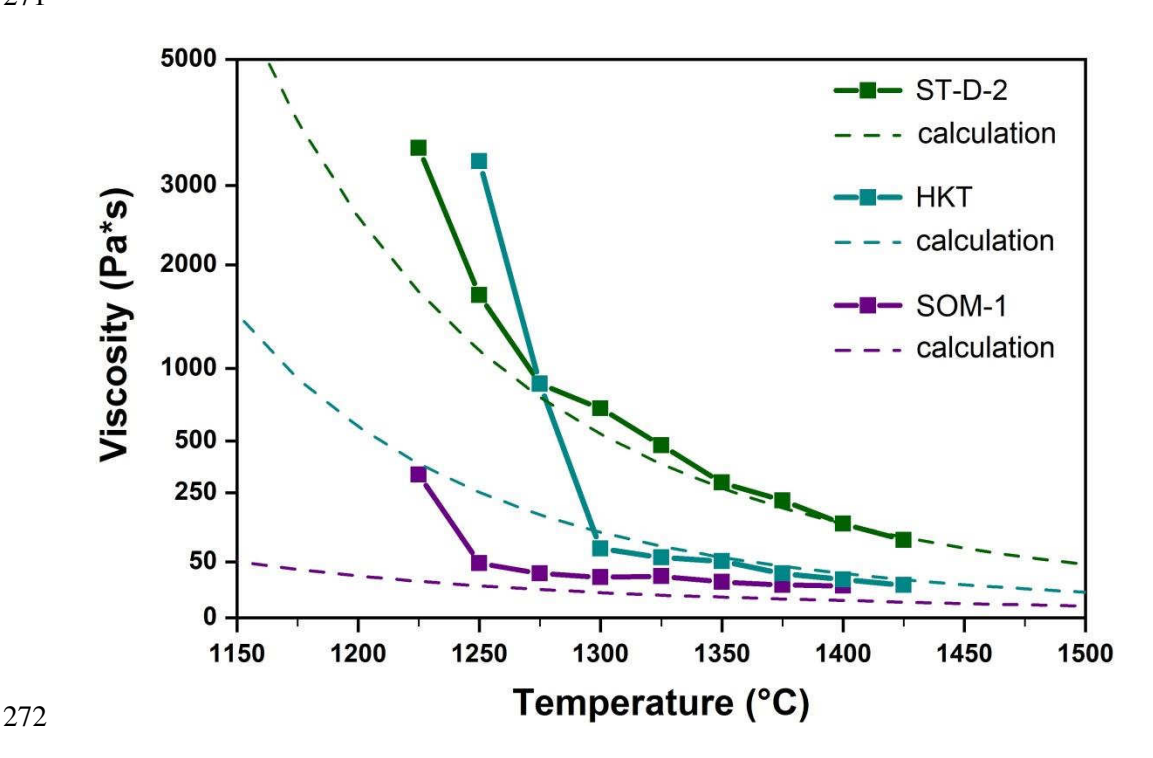


Figure 4: Comparison of stepwise measured viscosity of synthetic HKT slag, with viscosity modelling results executed with a viscosity model [2, 15, 35].

To gather a deeper insight into the crystallisation and the growth kinetics, HKT slag was chosen for a detailed viscosity investigation. An isothermal measurement at 1250 °C for 7 h of holding time was performed (Fig. 5). For silicate systems, the typical trend of a declining viscosity with higher rpm can be observed, as the rotating spindle disrupts the silicate network and reduces the viscosity. However, after approx. 170 min, a wide peak on the viscosity graph was observed, indicating a relatively higher resistance towards shear of the slag. After 310 min, the viscosity trend smoothened again. A sample cross section was prepared and microscopic analysis revealed the presence of crystals in the synthetic HKT slag (Fig. 5). A fully amorphous slag would appear glassy, but as the image displays, the slag appeared as turbid due to present crystals. Additional SEM and SEM-EDX analysis was performed on the crystallised slag. Fig. 5 displays elongated crystals in the viscosimetry crucible with a parallel orientation. The direction of orientation is parallel to the applied shear stress by the rotational spindle. Therefore, it can be assumed that the smoothened crystallisation peak occurred due to shear thinning behaviour by the orientation of elongated crystals. SEM-EDX mapping displays that the crystals are enriched in Al and Ca, but depleted in Mg, compared to the remaining slag. EDX point measurement indicated an anorthite composition of the crystals. The investigation of real HKT slag also revealed an immediate viscosity increase and the presence of crystals with anorthite composition [3].

275

276

277

278

279

280

281

282

283

284

285

286

287

288

289

290

291

292

293

294

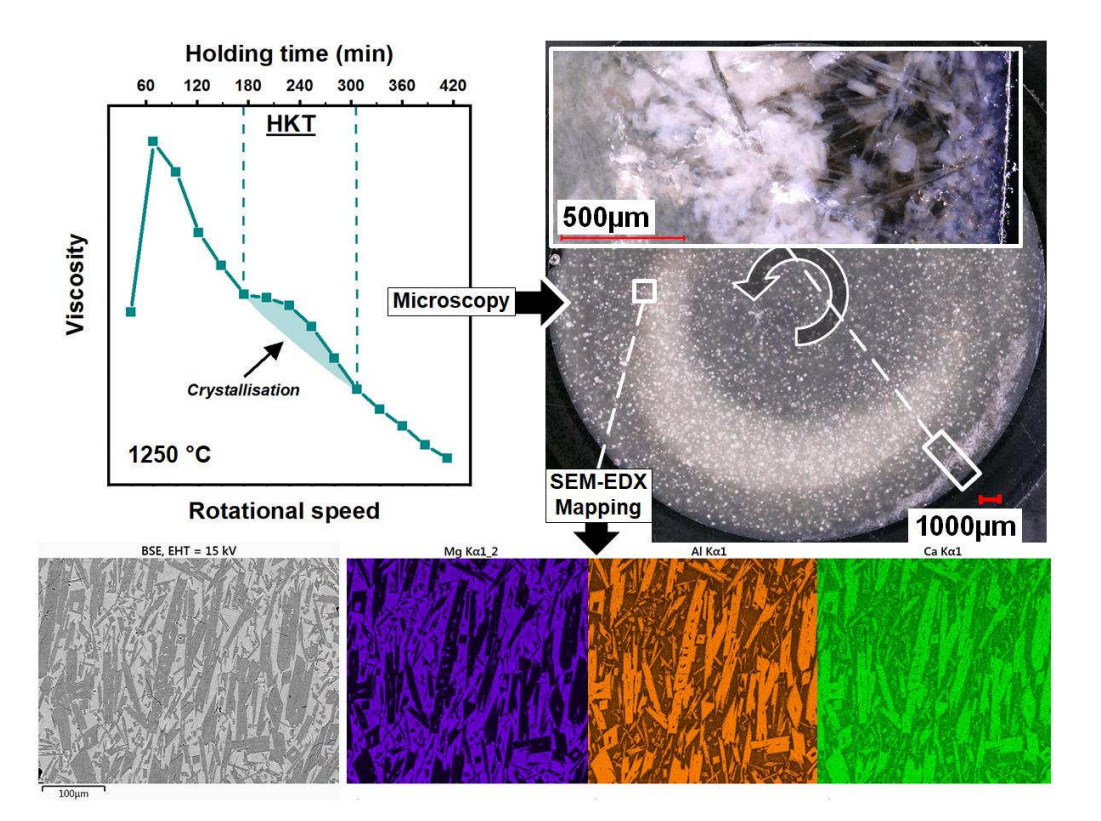


Figure 5: Viscosity data with crystallisation peak of an isothermal viscosity measurement at 1250 °C. The sample was analysed via digital microscopy and SEM-EDX. The elongated crystals showed anorthite composition.

It can be concluded that the viscosity behaviour and the crystallisation results of the synthetic slag are highly comparable with the real HKT slag. As described previously [26], a viscosity model for partially crystallised slags requires crystal morphology data. Since the impact of crystallisation on the viscosity was proven for the synthetic HKT slag, crystallisation of slags will be described by mainly referring to the HKT slag system in the following sections.

## 3.3 Phase determination by crystal structure analysis

The crystallisation behaviour of synthetic HKT slag was investigated under various temperature and time conditions by applying quenching experiments. Therefore, a total amount of 50 samples passed the quenching experiment. As the equilibrium calculation predicted, several phases are expected to grow in the slag. To determine these crystalline phases by their crystallographic properties, XRD measurements of a selection of representative samples is shown in the following. The chosen samples

represent temperatures of 1200 °C and 1100 °C with an associated holding time of 4 h (Fig. 6). The spectra were compared with several datasets, and two phases were identified to be present in the crystallised slags: anorthite and cristobalite. Sample spectra below 31° 2θ show a satisfactory accordance with the dataset peaks. Since the analysed samples were embedded into epoxy resin for subsequent SEM investigations, only a two-dimensional planar surface of the crystallised slag was analysed, to determine the spatial distribution of the grown crystals in the cross section area. The crystallographic orientation (hkl) was determined by XRD and then compared with the crystal orientations observed in the microscopic analysis.

At a higher temperature of 1200 °C, peak analysis revealed that anorthite crystallised

At a higher temperature of 1200°C, peak analysis revealed that anothrite crystallised preferably in orientations (130), ( $1\bar{3}1$ ) and ( $2\bar{4}0$ ) (Fig. 6). According to (130) and ( $2\bar{4}0$ ), anorthite crystal surfaces show orientations perpendicular to the c-axis of the crystal lattice. Anorthite peaks of the 1100 °C spectrum indicate further hkl such as (222), ( $20\bar{2}$ ) and (244). Along with the aforementioned indices, the crystal lattice distribution is more diverse.

The crystallographic orientation was correlated with the crystal morphologies and their spatial orientation by microscopic images. The associated samples are displayed

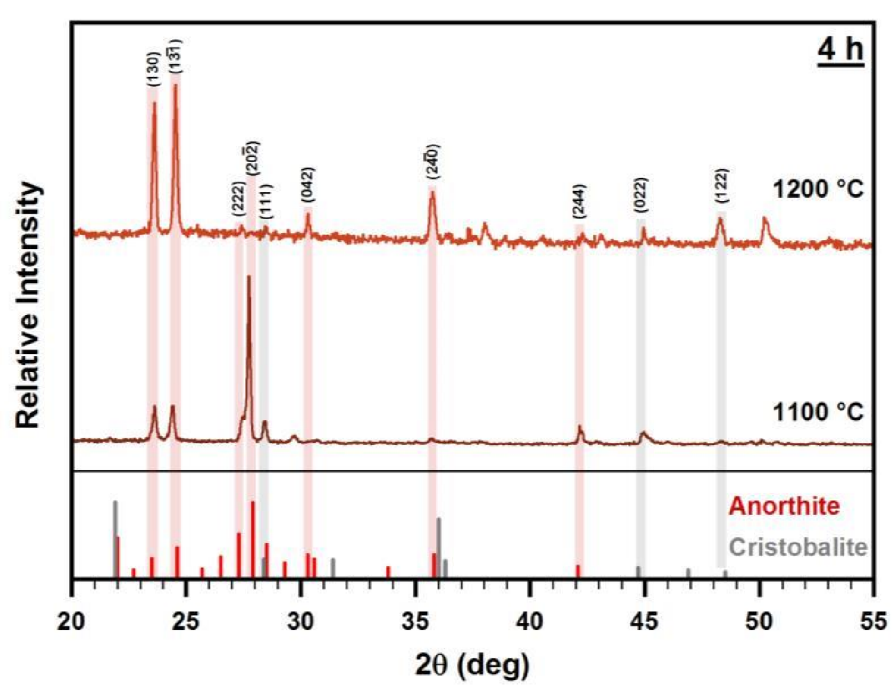


Figure 6: XRD spectra of two representative samples quenched at 1200  $^{\circ}$ C and 1100  $^{\circ}$ C after a holding time of 4 h each.

in Fig. 7. The microscopic image of the sample cross section (1200 °C, 4 h holding time), for example, indicates that crystallisation is dominated by elongated crystals in an overall threadlike structure and oriented parallel to the cross section (Figure 7a). XRD peaks show similarities of anorthite lattice orientations (perpendicular to c-axis, Fig. 6) and microscopic images display a preferred crystal orientation in the same sample. Thus, an overall conclusion of both results is legitimised. Therefore, it can be concluded that anorthite crystals show an elongated growth in direction of the crystals c-axis.

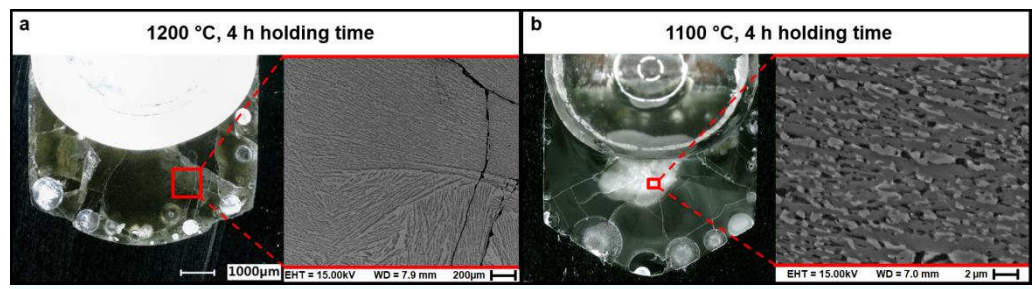


Figure 7: Microscopic view of the cross sections of quenched HKT slag samples at  $1200~^{\circ}$ C and  $1100~^{\circ}$ C. The corresponding holding time was four hours each.

As XRD spectra were further compared with ICSD datasets, a vague accordance with cristobalite was found. Regarding both spectra (Fig. 6), only few peaks can be correlated unambiguously. Therefore, the overall presence of cristobalite cannot be concluded undoubtedly. Other phases such as clinopyroxene and cordierite (Fig. 6) are not considered in the XRD spectra. Quenched samples show intensified crystallisation as the holding time increased. Therefore, four representative samples with the maximum holding time of 24 hours were chosen to represent equilibrium conditions in the HKT slag. Slag powder was preferably used to enhance the spectra quality, compared with the embedded samples mentioned before. As displayed in Fig. 8, all four spectra show a comparable course, indicating similar crystalline phases. At 1150 °C, anorthite is the dominant phase, as already stated at shorter holding times. However, other phases such as SiO<sub>2</sub> (including cristobalite, high quartz and low quartz), clinoenstatite and augite (both belong to the Clinopyroxene group) can be correlated with the spectrum (Fig. 8). Regarding the lower temperatures, the peak correlation of SiO<sub>2</sub>, augite and clinoenstatite becomes more trustworthy, likewise their

peak intensity increases. These three phases preferably crystallise at lower temperatures, while anorthite is always present. The comparison of Figs. 6 and 8 clearly indicates that the evolution of crystallised phases is strongly influenced by the sample holding time and therefore kinetics. Accordingly, an extended period of time is necessary for the synthetic HKT slag system to reach a (quasi-)equilibrium state.

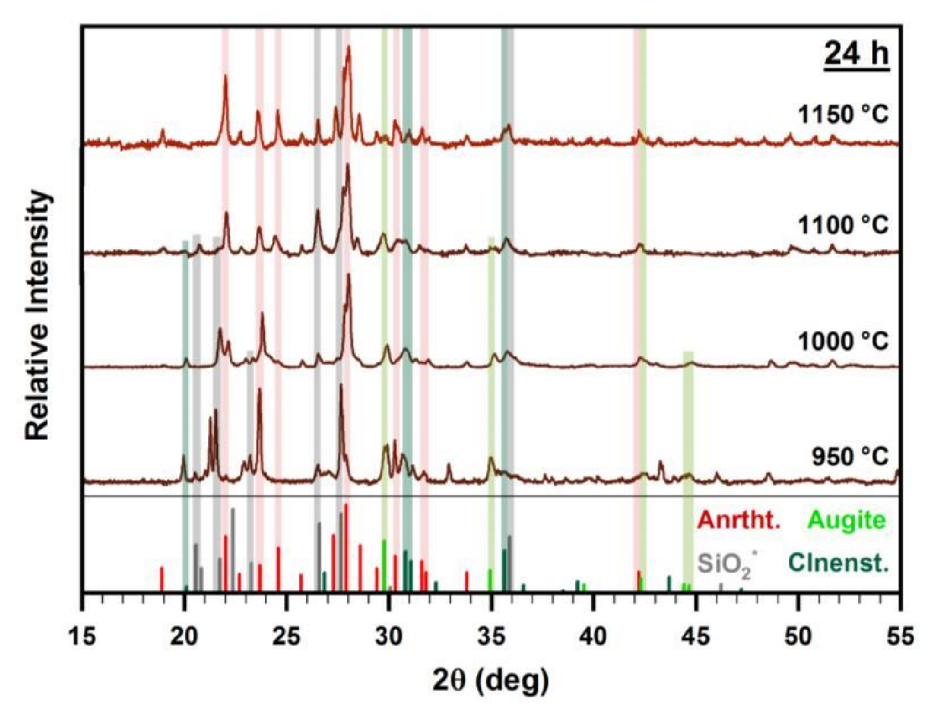


Figure 8: XRD spectra of four representative samples quenched at 1150, 1100, 1000 and 950 °C after a holding time of 24 hours each. The correlated datasets are: anorthite (red), SiO<sub>2</sub>\* (including cristobalite, quartz and quartz low, grey), augite (light green), clinoenstatite (dark green). Datasets derive from ICSD

3.4 Evolution of crystallisation

Similar to the crystal structure analysis, the numerous samples from the quenching experiment were used to analyse the evolution of crystallisation with respect to different time and temperature steps. To gather high resolution images of the crystallised phases and their composition, SEM and SEM-EDX analysis was performed.

The collection of all crystallised samples was analysed using SEM and SEM-EDX. By comparing the results, some general tendencies could be observed in the samples. In consensus with the crystallisation theory [39], at higher temperatures larger crystals

371 that are less in number formed, while lower temperatures allowed for numerous 372 crystals to form, displaying a limited crystal size (Fig. 9). 373 The sample quenched at 1250 °C contains few crystals with lengths varying from 374 several hundred micrometres up to a few millimetres. The corresponding SEM images 375 in Fig. 9a display a detailed view on their elongated, hopper shapes. These crystals 376 also show partial disintegration into single quadrangular fragments. Furthermore, 377 EDX mapping reveals an enrichment of Al and Ca in that phase, while Si is depleted 378 compared with the surrounding slag. Mg and Fe are absent in the phase (Fig. 9a). 379 At a slightly reduced temperature (1200 °C), quenched slags show a higher number of crystals in a threadlike pattern. They are elongated as well, and their inner structure is 380 381 jagged. By taking occasional crystal shape deviations into account, the crystal 382 morphologies are comparable between 1250 °C and 1200 °C. Thus, the crystallised phases at both temperatures are likely identical. Large grown, fragmented crystals 383 384 were also found at 1300 °C (24 h of holding time) and threadlike crystal arrangements were observed as well at 1150 °C (1, 4, 7 and 24 h). Thus, this elongated phase is 385 386 dominant between 1150 °C and 1300 °C, showing also comparable morphologies.

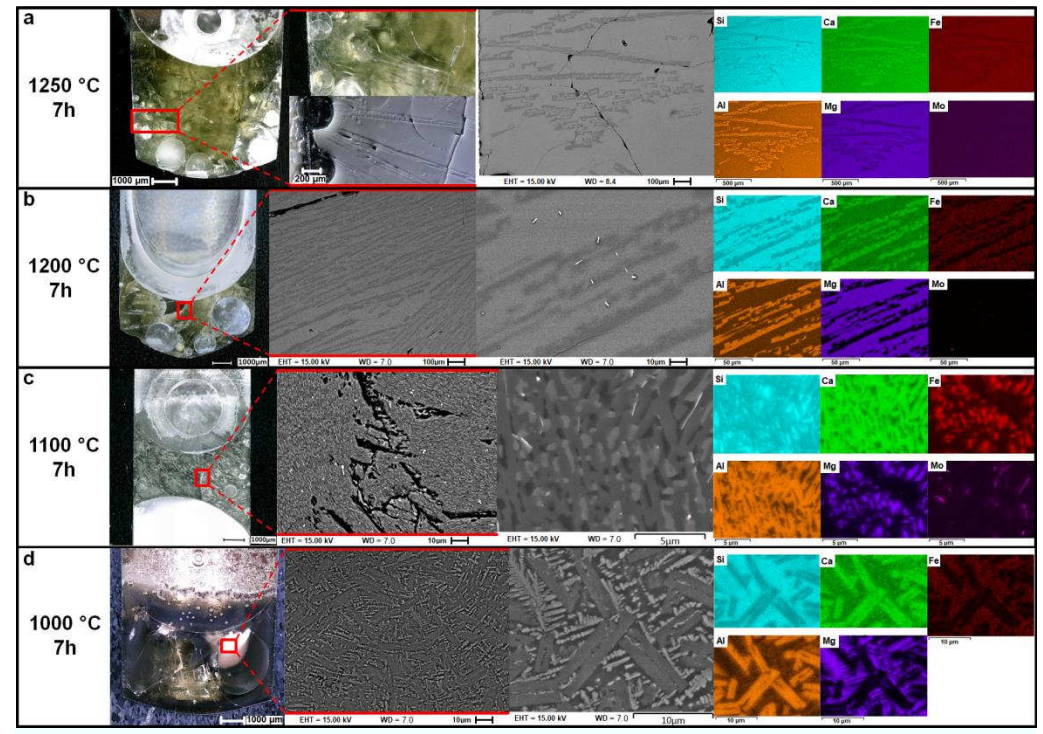


Figure 9: Crystallisation documented by SEM and SEM-EDX mapping in representative samples, quenched at 1250  $^{\circ}$ C, 1200  $^{\circ}$ C, 1100  $^{\circ}$ C and 1000  $^{\circ}$ C, with a holding time of 7 hours each.

However, from 1100 °C downwards, crystallisation shows alternate characteristics. The microscopic image indicates that the complete slag is no longer vitreous (Fig. 9c). Therefore, SEM images display the appearance of two different crystalline phases. The first phase has an elongated shape with lengths of a maximum of approx.  $20~\mu m$ . The second phase formed with xenomorphic shapes in the gaps between the elongated phase. The xenomorphic crystals seem not to disrupt the growth of the elongated crystals, indicating that elongated phase growth was finished before the xenomorphic phases nucleated. By taking chemical information from the EDX-mapping into account, the elongated phase shows the same element distribution as the higher temperate elongated phases. Therefore, it is likely that both phases are identical, in spite of a reduction in crystal sizes.

The xenomorphic phase displays an intense Si signal but lacks of other elements. The lowest temperature of 1000 °C led to the forming of a cloud-shaped crystallisation zone that has a different inner structure (Fig. 9d) compared to that at 1100 °C. This zone consists of H-shaped, rectangular crystals with lengths of 10-35  $\mu$ m,

perpendicular orientated dendrites (5-35  $\mu$ m length), and some xenomorphic crystals (<15  $\mu$ m diameter) that formed in the gaps between the other two phases. Regarding the EDX-mappings, the H-shaped phase indicates the same chemical distribution as the elongated phase described before. The xenomorphic phase shows strong similarities in terms with the xenomorphic phase described at 1100 °C.

Additionally, the dendritic phase was firstly documented at 1000 °C. EDX-mapping indicates a significant enrichment of Mg, as well as a depletion of Al and Ca. The dendrite phase growth characteristics clearly indicate that they also evolved in the gaps between the H-shaped crystals. In terms of the growth order, the dendrite-phase grew after the H-shaped phase and seemingly before the xenomorphic phase.

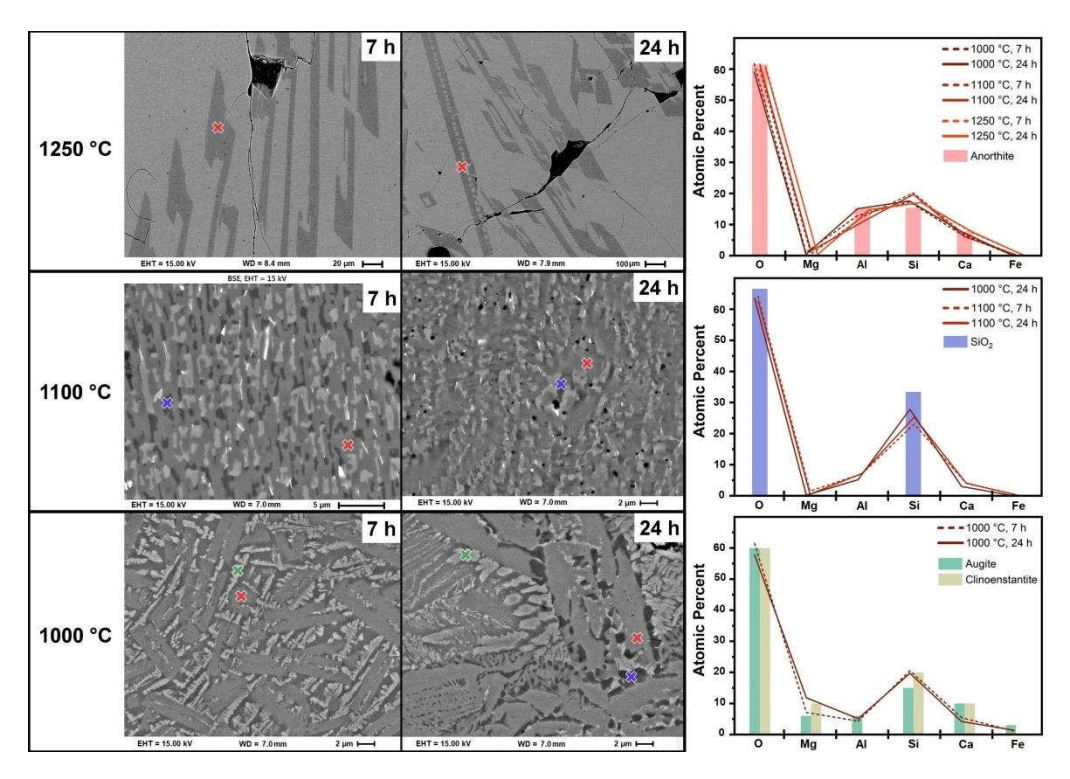


Figure 10: Representative SEM images of HKT slag samples at 1000, 1100 and 1250  $^{\circ}$ C with holding times of 7 and 24 h. Anorthite, SiO<sub>2</sub> and clinopyroxene phases are determined by SEM-EDX measurements.

The before mentioned phases were identified using single SEM-EDX point measurements, as displayed in Fig. 10. The first elongated Al- and Ca- enriched phase displays anorthite composition. EDX measurements of crystal compositions are consistent in all displayed samples. It follows that anorthite, in combination with the XRD measurements, is clearly identified as the Al- and Ca- rich, elongated phase. Fig.

10 reveals that the xenomorphic crystal phase consists of Si and O. Therefore, the xenomorphic phase was determined to be SiO<sub>2</sub>, though SEM-EDX measurements also indicate Al and Ca to be present in that phase. This divergence can be explained by the tiny size of the analysed crystals and a distortion of the electron beam by the surrounding slag (Fig. 10).

The third phase described is the Mg-rich dendrite phase, documented at 1000 °C. A comparison of the slag with augite and clinoenstatite indicates that the overall fit is satisfactory. As can be seen in Fig. 10, the dendritic phase in both samples (7 h and 24 h) shows minor deviations in its Mg content. By also taking diopside (CaMgSi<sub>2</sub>O<sub>6</sub>) and pigeonite ((Mg,Fe,Ca)<sub>2</sub>Si<sub>2</sub>O<sub>6</sub>) into account, clinopyroxenes face a miscibility of Ca, Mg, Fe and Al. Another visible finding in Fig. 10 is the fact that in terms of the crystal size, the clinopyroxene phase grew slightly in size as the holding time increased. Furthermore, its crystal shape partially transformed from a dendritic shape to a polygonal shape during that growth process, indicating that a crystallographic preferred structure was about to form out of the dendrite shape. Compared with a recent work [26], the crystallisation products display less symmetric shapes.

#### 3.5 Crystal morphology and quantification - anorthite

As anorthite is the first crystallizing phase causing the observed viscosity increase, it is most relevant for gasifier operation. The elongated crystal morphology of anorthite described in this study is in very good agreement with anorthite morphology described in the literature. Anorthite crystals with a comparable morphology as the one shown in Fig. 11a,b,c were also observed in the ST-D-2 and SOM-1 slag, which is why all three slag systems were used to quantify an overall anorthite morphology.

In a study by Sato [40], plagioclase crystals grew during a viscosity measurement of a subliquidus magma. Since anorthite is part of the solid solution of plagioclase, the morphology of plagioclase and anorthite can be treated as similar. The observed crystals are elongated as well, as can be seen in Fig. 11d. In the recent study of Seebold, real ST-D-2 slag was investigated on the viscosity and large anorthite crystals were found in the slag (Fig. 11e) [3]. The comparison of both anorthite

morphologies from synthetic HKT and real ST-D-2 slag (Fig. 11c,e) clearly display that the elongated morphology is identical, even though the slags have different compositions (and real ST-D-2 contains also alkalis). Further studies also revealed the elongated shape of anorthite crystals (Fig. 11f,g) [41, 42]. Additionally, other studies observed the crystallisation of elongated anorthite or plagioclase crystals [40, 43-46]. One century ago, Goldschmidt collected early findings on crystal morphologies [47] and also defined an elongated anorthite shape (Fig. 11h).

These overarching coincidences prove firstly that the abundance of anorthite in slag and natural systems gives high relevance to its quantification. Secondly, anorthite morphology is not influenced by the composition of the investigated systems (different slags and magmas) or the experimental procedure and can therefore be seen as characteristic for the anorthite phase.

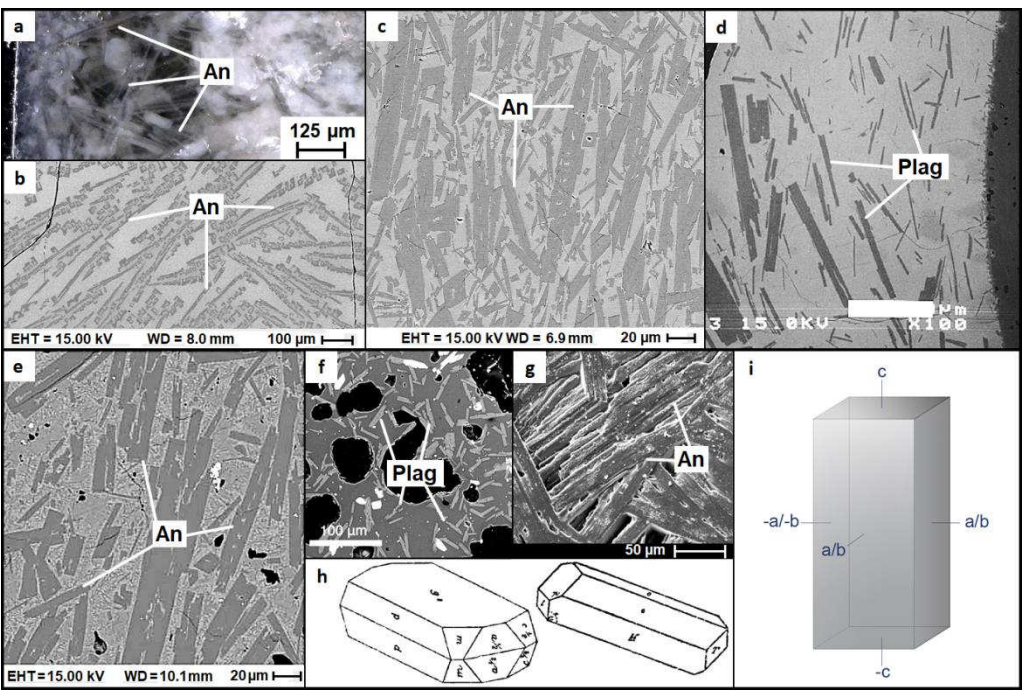


Figure 11: Selection of documented anorthite morphologies. a) microscopic image of anorthite crystals on the wall of the previously investigated viscosimetry crucible, b) crystallised anorthite from the quenching experiment (1250 °C, 24 h), c) SEM image of orientated anorthite crystals due to spindle rotation (same sample like a)), d) crystallised anorthite during viscosity measurement of subliquidus [41], e) crystallised anorthite in real HKT slag [39], f) crystallised plagioclase in H<sub>2</sub>O and H<sub>2</sub>O-CO<sub>2</sub>-saturated magmas [41], g) crystallised anorthite in quenched coal ash slag [42], h) anorthite morphologies as described by Goldschmidt (1922) [47], i) generalised tetragonal prism morphology for the anorthite crystal quantification.

As a result of the uniformity of anorthite (or plagioclase) crystals, a generalised anorthite morphology was created as a basis for the quantification (Fig. 11i). The idealised crystal was defined as a tetragonal prism with a varying prism length. Since the XRD investigations revealed that the elongated axis must be represented by the caxis, crystallographic spatial axis could be identified (Fig. 11i). As the a- and b-axis are treated equally, the whole crystal morphology can be ascertained by the generalised width. The anorthite morphology data for the generalised tetragonal prism shape are displayed in the following figures. By comparing anorthite tetragonal prism length data, a clear tendency can be seen to form large crystals at higher temperatures and smaller ones at intermediate and low temperatures (Fig. 12). Crystallisation theory specifies crystal growth to be dominant at high temperatures and nucleation at low temperatures, which accounts for the anorthite phase [48, 49]. In general, anorthite crystals grew comparably large in the HKT and SOM-1 slag. Especially the sharp decline in anorthite mean length until 1100 °C is similar. ST-D-2 slag in contrast, generally displays lower anorthite lengths (Fig. 12). Below 1100 °C, anorthite mean length in HKT slags displays fluctuations on a low double-digit µm-scale, while SOM-1 and ST-D-2 length constantly decline further. The corresponding quantile data can be seen as channel margins in which anorthite crystals highly likely form in the slags. To uniform anorthite length data, it was decided to define average anorthite length data. Therefore, the individual slag mean lengths and quantiles were condensed by averaging between the three slag systems. Fig. 12 displays that the average anorthite length can be divided into two major regimes: 1250 °C to 1100 °C and 1100 °C to 900 °C. At 1250 °C, anorthite mean length was determined to 1471 µm with a bandwidth of 344-1888 µm. The margin of the high temperature regime at 1100 °C is marked by an averaged anorthite mean length of 8 µm and quantiles of 20.3 µm and 3.5 µm, respectively.

474

475

476

477

478

479

480

481

482

483

484

485

486

487

488

489

490

491

492

493

494

495

496

497

498

499

500

501

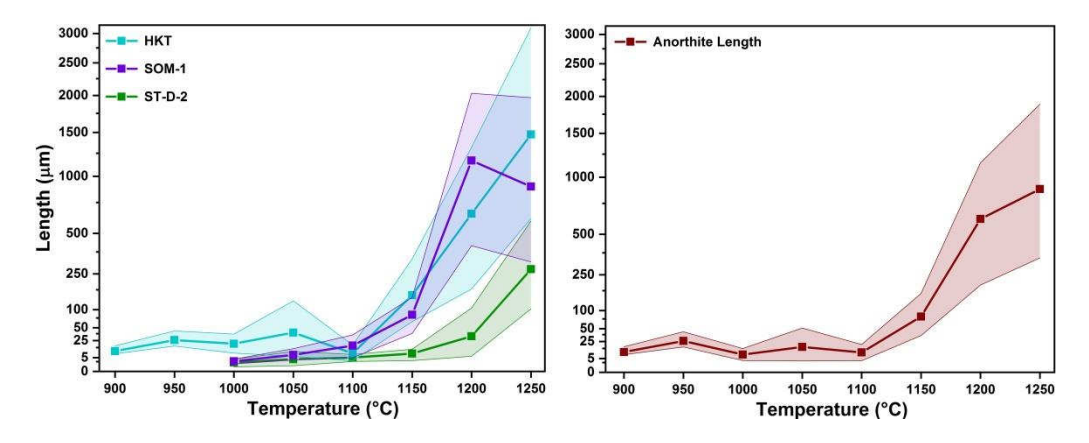


Figure 12: 90<sup>th</sup>/10<sup>th</sup> quantile and mean anorthite crystal length (left) and averaged 90<sup>th</sup>/10<sup>th</sup> quantile and averaged mean anorthite crystal length (right) with respect to the quenching temperature of ST-D-2, HKT, and SOM-1 slag.

502

503

504

505

506

507

508

509

510

511

512

513

514

515

516

517

518

519

520

521

522

523

524

525

Anorthite tetragonal prism is furthermore described by the width (a-, b-axis) of the crystal. The deviation of the length and the width results in the crystal aspect ratio. The aspect ratio data of the three analysed slag systems are displayed in Fig. 13. The overall AR graphs follow a general trend: higher temperatures lead to more elongated anorthite crystals. HKT slag produced anorthite crystals with the highest mean aspect ratio of 29.6 (1200 °C). SOM-1 slag reaches a maximum of 19.2 (1200 °C) and ST-D-2 of 16.2 (1250 °C). Similar to the mean anorthite length, ST-D-2 anorthite crystals have the lowest aspect ratio, compared to the other slag systems. As can be seen at low temperatures (1000 °C), the deviation between ST-D-2, HKT, and SOM-1 slag narrows and anorthite crystals face a similar elongation (Fig. 13). Accordingly, the aspect ratio of anorthite crystals in all three slags have a better overlap, compared with the crystal length data, shown before (Fig. 13). According to the averaged anorthite length, anorthite aspect ratio was also averaged based on the three slag systems. The averaged mean aspect ratio, as well as the 90th and 10<sup>th</sup> quantiles can be seen in Fig. 13. The fundamental trend of larger AR at higher temperatures is present for the averaged aspect ratio data, likewise. At the lowest temperature of 900 °C, the averaged mean aspect ratio is approx. 2.5 (only HKT data). Above 950 °C, aspect ratio data begin to rise almost perfectly constant until the maximum investigated temperature of 1250 °C. The bandwidth of the maximum and

minimum values is comparably narrow, indicating a higher homogeneity of anorthite crystals aspect ratio, compared with the absolute lengths. Surprisingly, the fine-grained, cloud-shaped crystallisation did not have an influence on anorthite aspect ratio, in contrast to the crystal length (below and above 1100 °C, Fig. 13).

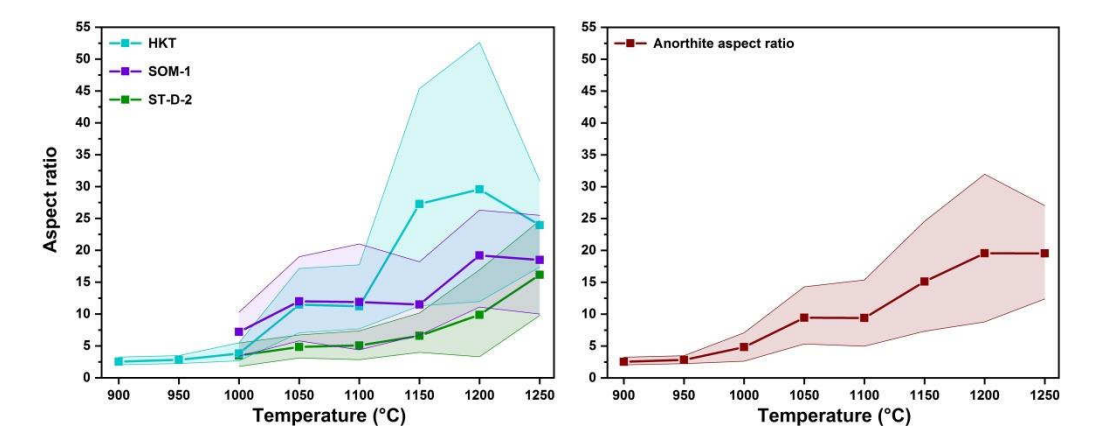


Figure 13: 90<sup>th</sup>/10<sup>th</sup> quantile and mean anorthite crystal aspect ratio (left) and averaged 90<sup>th</sup>/10<sup>th</sup> quantile and averaged mean anorthite crystal aspect ratio (right) with respect to the quenching temperature of ST-D-2, HKT, and SOM-1 slag.

#### 4 Conclusion

In this study, viscosity and crystallisation characteristic with special focus on the anorthite (CaAl<sub>2</sub>Si<sub>2</sub>O<sub>8</sub>) phase were investigated for three synthetic coal slags (ST-D-2, HKT, SOM-1). For this purpose, high temperature viscosimetry and quenching experiments were applied. In the end, anorthite was defined as the major crystallising phase. A generalised anorthite morphology was defined and its morphology was quantified. Anorthite morphology data can be used in a future viscosity model for partly crystallised slags [26].

The viscosity measurements reveal that the measured viscosity of slags aligns well with calculation results, using the model of Wu et al. [2, 15, 35, 50], as long as the slags are completely molten and display Newtonian behaviour. An isothermal viscosity measurement of HKT slag revealed an influence of crystallisation on the viscosity course. Analysis of the sample revealed the presence of elongated crystals with anorthite composition. Therefore, the crystallisation of anorthite has clear

550 influence on the slag viscosity. This is why its crystallisation behaviour was further 551 investigated exemplarily for HKT by a series of quenching experiments. 552 In accordance with thermochemical calculations, quenched samples proofed a crystal 553 phase dominance of anorthite [44]. Clinopyroxene (AB(Si,Al)<sub>2</sub>O<sub>6</sub>) and SiO<sub>2</sub> (SiO<sub>2</sub>) 554 were also documented in the experiments, though the corresponding temperatures of 555 occurrence varied between the calculations and the experiments. 556 Ouenched samples clearly indicated the presence of elongated crystals, similar to the 557 viscosimetry sample. XRD analysis identified the elongated crystal phase to be anorthite. The primary growth axis could be identified as the crystallographic c-axis of 558 559 the anorthite crystals Additional SEM and SEM-EDX analysis of the quenching 560 samples uncovered variations of the anorthite shape. In tendency, lower temperatures 561 led to the formation of smaller anorthite crystals, thus its elongated nature remained 562 similar. Since anorthite was identified as the dominant phase in all slag systems and since its 563 564 outlook showed a similar shape, a generalised anorthite morphology was defined. Due 565 to its elongated nature, anorthite crystals were defined as a tetragonal prism, with 566 variable dimensions. Based on the isothermal quenching experiments of all three slag systems, anorthite crystals were quantified on their length and their aspect ratio. 567 568 Anorthite morphology quantification revealed higher crystal lengths above 1100 °C, 569 but comparable lengths at temperatures below. The trend to form larger crystals at 570 higher temperatures is in agreement with the general crystallisation theory [48, 49]. 571 Furthermore, anorthite aspect ratio revealed a clear trend of forming crystals with 572 higher aspect ratio with an increase of the applied temperature. 573 In a previous work, the approach of using crystal morphology data for a viscosity 574 model for partly crystallised slags was introduced and morphology datasets for 575 melilite and olivine were presented [26]. Anorthite morphology data presented in this 576 study serve a valuable addition and can be applied in a future viscosity model for

577

partly crystallised slags [26].

# Acknowledgement

580 The work described in this paper has been performed in the framework of the

581 HotVeGas Project supported by Bundesministerium für Wirtschaft und Energie (FKZ

582 0327773).

579

- 584 [1] Y. Huang, S. Rezvani, D. McIlveen-Wright, A. Minchener, N. Hewitt, Techno-
- economic study of CO2 capture and storage in coal fired oxygen fed entrained flow
- 586 IGCC power plants, Fuel Process. Technol., 89 (2008) 916-925
- 587 <u>https://doi.org/10.1016/j.fuproc.2008.03.002</u>.
- 588 [2] G. Wu, E. Yazhenskikh, K. Hack, E. Wosch, M. Müller, Viscosity model for oxide
- melts relevant to fuel slags. Part 1: Pure oxides and binary systems in the system
- 590 SiO<sub>2</sub>-Al<sub>2</sub>O<sub>3</sub>-CaO-MgO-Na<sub>2</sub>O-K<sub>2</sub>O, Fuel Process. Technol., 137 (2015) 93-103.
- 591 <a href="http://dx.doi.org/10.1016/j.fuproc.2015.03.025">http://dx.doi.org/10.1016/j.fuproc.2015.03.025</a>.
- 592 [3] S. Seebold, G. Wu, M. Müller, The influence of crystallization on the flow of coal
- 593 ash-slags, Fuel, 187 (2017) 376-387. <a href="http://dx.doi.org/10.1016/j.fuel.2016.09.078">http://dx.doi.org/10.1016/j.fuel.2016.09.078</a>.
- 594 [4] W.J. Song, Y.M. Sun, Y.Q. Wu, Z.B. Zhu, S. Koyama, Measurement and Simulation of Flow Properties of Coal Ash Slag in Coal Gasification, Aiche Journal,
- 596 57 (2011) 801-818. http://dx.doi.org/10.1002/aic.12293.
- 597 [5] J. Eurling, J. Ploeg, Process Performance of the SCGP at Buggenum IGCC, in:
- 598 Gasification Technologies Conference, San Francisco, California, 1999, pp. 21.
- 599 [6] P. Holmgren, M. Broström, R. Backman, Slag Formation during Entrained Flow
- Gasification: Silicon-Rich Grass Fuel with a KHCO<sub>3</sub> Additive, Energy & Fuels, 32
- 601 (2018) 10720-10726. 10.1021/acs.energyfuels.8b02545.
- 602 [7] D.H. Schwitalla, A.M. Bronsch, M. Klinger, S. Guhl, B. Meyer, Analysis of solid
- phase formation and its impact on slag rheology, Fuel, 203 (2017) 932-941.
- 604 dx.doi.org/10.1016/j.fuel.2017.04.092.
- [8] S. Seebold, M. Eberhard, G. Wu, E. Yazhenskikh, D. Sergeev, T. Kolb, M. Müller,
- Thermophysical and chemical properties of bioliq slags, Fuel, 197 (2017) 596-604.
- 607 <u>https://doi.org/10.1016/j.fuel.2017.02.027</u>.
- 608 [9] Q. Ren, Y. Zhang, Y. Long, Z. Zou, J. Pei, Crystallisation behaviour of blast
- 609 furnace slag modified by adding fly ash, Ceramics International, 44 (2018) 11628-
- 610 11634. https://doi.org/10.1016/j.ceramint.2018.03.237.
- 611 [10] W. Xuan, J. Zhang, D. Xia, The influence of MgO on the crystallization
- 612 characteristics of synthetic coal slags, Fuel, 222 (2018) 523-528
- 613 https://doi.org/10.1016/j.fuel.2018.02.197.
- 614 [11] H. Shaw, Viscosities of magmatic silicate liquids; an empirical method of
- prediction, American Journal of Science, 272(9) (1972) 23.
- 616 <a href="http://dx.doi.org/10.2475/ajs.272.9.870">http://dx.doi.org/10.2475/ajs.272.9.870</a>.
- [12] G. Urbain, Etude experimentale de la viscosite des silicoalumineux liquides et
- 618 essai d'interpretation structurale, in, Université de Paris, Paris, 1972,
- 619 [13] A. Kondratiev, E. Jak, Review of experimental data and modeling of the
- 620 viscosities of fully liquid slags in the Al2O3-CaO-'FeO'-SiO2 system, Metallurgical
- and Materials Transactions B, 32 (2001) 1015-1025. dx.doi.org/10.1007/s11663-001-
- 622 0090-y.
- 623 [14] I. Avramov, C. Rüssel, R. Keding, Effect of chemical composition on viscosity of
- oxide glasses, J. Non-Cryst. Solids, 324 (2003) 29-35. https://doi.org/10.1016/S0022-
- 625 3093(03)00230-8.
- 626 [15] G. Wu, E. Yazhenskikh, K. Hack, M. Müller, Viscosity model for oxide melts
- relevant to fuel slags. Part 2: The system SiO<sub>2</sub>–Al<sub>2</sub>O<sub>3</sub>–CaO–MgO–Na<sub>2</sub>O–K<sub>2</sub>O, Fuel
- 628 Process. Technol., 138 (2015) 520-533. https://doi.org/10.1016/j.fuproc.2015.06.031.
- 629 [16] Z. Shen, R. Li, Q. Liang, J. Xu, H. Liu, Effect of Cooling Process on the
- 630 Generation and Growth of Crystals in Coal Slag, Energy & Fuels, 30 (2016) 5167-
- 631 5173. https://doi.org/10.1021/acs.energyfuels.5b02625.
- 632 [17] Z. Shen, Q. Liang, J. Xu, Z. Dai, H. Liu, Study on the two-dimensional micro-
- 633 scale crystal growth of a coal slag, Fuel, 205 (2017) 24-33
- 634 https://doi.org/10.1016/j.fuel.2017.05.051.
- 635 [18] H.P. Yuan, Q.F. Liang, X. Gong, Crystallization of Coal Ash Slags at High
- Temperatures and Effects on the Viscosity, Energy & Fuels, 26 (2012) 3717-3722.
- 637 https://doi.org/10.1021/ef201894p.
- 638 [19] Z. Liu, L.G. Chen, B. Blanpain, M. Guo, Effect of Crystallization on the Abrupt
- 639 Viscosity Increase during the Slag Cooling Process, ISIJ Int., 58 (2018) 1972-1978.
- 640 https://doi.org/10.2355/isijinternational.ISIJINT-2018-176.

- [20] W. Xuan, K.J. Whitty, Q. Guan, D. Bi, Z. Zhan, J. Zhang, Influence of CaO on
- 642 Crystallization Characteristics of Synthetic Coal Slags, Energy & Fuels, 28 (2014)
- 643 6627-6634. https://doi.org/10.1021/ef501215u.
- 644 [21] W. Xuan, K.J. Whitty, Q. Guan, D. Bi, Z. Zhan, J. Zhang, Influence of
- 645 SiO<sub>2</sub>/Al<sub>2</sub>O<sub>3</sub> on crystallization characteristics of synthetic coal slags, Fuel, 144 (2015)
- 646 103-110. https://doi.org/10.1016/j.fuel.2014.11.091.
- 647 [22] Z. Liu, L. Zhang, A. Malfliet, B. Blanpain, M. Guo, Non-Newtonian behavior of
- solid-bearing silicate melts: An experimental study, J. Non-Cryst. Solids, 493 (2018)
- 649 65-72. https://doi.org/10.1016/j.jnoncrysol.2018.04.042.
- 650 [23] G. Wu, Modelling and Experimental Validation of the Viscosity of Liquid Phases
- 651 in Oxide Systems Relevant to Fuel Slags, in: Fakultät für Maschinenwesen,
- Rheinisch-Westfälische Technische Hochschule Aachen, Aachen, 2015,
- 653 [24] S. Esfahani, M. Barati, Effect of slag composition on the crystallization of
- 654 synthetic CaO–SiO<sub>2</sub>–Al<sub>2</sub>O<sub>3</sub>–MgO slags: Part I- Crystallization behavior, J. Non-Cryst.
- 655 Solids, 436 (2016) 35-43. https://doi.org/10.1016/j.jnoncrysol.2015.12.011.
- 656 [25] G.-H. Wen, H. Liu, P. Tang, CCT and TTT Diagrams to Characterize
- 657 Crystallization Behavior of Mold Fluxes, Journal of Iron and Steel Research,
- 658 International, 15 (2008) 32-37. https://doi.org/10.1016/S1006-706X(08)60140-5.
- 659 [26] J.P. Schupsky, G. Wu, M. Guo, M. Müller, Crystallisation characteristics and
- crystal phase quantification of a synthetic lignite gasifier slag system, Fuel Process.
- Technol., 201 (2020) https://doi.org/10.1016/j.fuproc.2020.106345.
- 662 [27] T. Melchior, M. Bläsing, G. Pütz, M. Müller, Surface tension measurements of
- 663 coal ash slags under reducing conditions at elevated pressures, Fuel, 90 (2011) 280-
- 664 287. <a href="https://doi.org/10.1016/j.fuel.2010.07.051">https://doi.org/10.1016/j.fuel.2010.07.051</a>.
- [28] J.P. Schupsky, M. Guo, B. Blanpain, M. Müller, Investigations on Crystallization
- Processes of Three Oxidic Gasifier Slag Systems, Journal of Energy Resources
- 667 Technology, 142 (2020) 9. 10.1115/1.4046145.
- 668 [29] D.P. Kalmanovitch, J. Williamson, Crystallization of Coal Ash Melts, in: K.S.
- Vorres (Ed.) Mineral Matter and Ash in Coal, ACS Symposium Series, 1986, pp. 234-
- 670 255. https://doi.org/10.1021/bk-1986-0301.ch018.
- [30] W.W. Xuan, K.J. Whitty, Q.L. Guan, D.P. Bi, J.S. Zhang, Influence of isothermal
- temperature and cooling rates on crystallization characteristics of a synthetic coal slag,
- 673 Fuel, 137 (2014) 193-199. https://doi.org/10.1016/j.fuel.2014.07.092.
- 674 [31] W. Xuan, Qian Wangb, Jiansheng Zhangb, D. Xia, Influence of silica and
- alumina (SiO<sub>2</sub>+Al<sub>2</sub>O<sub>3</sub>) on crystallization characteristics of synthetic coal slags, Fuel,
- 676 189 (2017) 39-45. https://doi.org/10.1016/j.fuel.2016.10.081.
- 677 [32] C.W. Bale, E. Bélisle, P. Chartrand, S.A. Decterov, G. Eriksson, A.E. Gheribi, K.
- Hack, I.H. Jung, Y.B. Kang, J. Melançon, A.D. Pelton, S. Petersen, C. Robelin, J.
- 679 Sangster, P. Spencer, M.A. Van Ende, FactSage thermochemical software and
- 680 databases, 2010–2016, Calphad, 54 (2016) 35-53.
- 681 https://doi.org/10.1016/j.calphad.2016.05.002.
- [33] K. Hack, T. Jantzen, M. Müller, E. Yazhenskikh, G. Wu, A novel thermodynamic
- database for slag systems and refractory materials, in: Proceedings of the 5<sup>th</sup>
- 684 International Congress on the Science and Technology of Steelmaking, Dresden,
- 685 Germany, 2012,
- 686 [34] T. Nentwig, Experimentelle Bestimmung und numerische Simulation von
- 687 Viskositäten in Schlackesystemen unter Vergasungsbedingungen, in: Fakultät für
- Maschinenwesen, Rheinisch-Westfälische Technische Hochschule Aachen, Aachen,
- 689 2011
- 690 [35] G. Wu, S. Seebold, E. Yazhenskikh, J. Tanner, K. Hack, M. Müller, Slag mobility
- 691 in entrained flow gasifiers optimized using a new reliable viscosity model of iron
- 692 oxide-containing multicomponent melts, Applied Energy, 236 (2019) 837-849.
- 693 <u>https://doi.org/10.1016/j.apenergy.2018.11.100</u>.
- 694 [36] J.P. Schupsky, M. Guo, B. Blanpain, M. Müller, The Impact of Sample
- 695 Homogeneity, Crucible Material, and Oxygen Partial Pressure on the Crystallization
- 696 of Fe-Rich Oxidic Slag in CLSM Experiments, Journal of Sustainable Metallurgy,
- 697 (2020)

- 698 [37] J. Nakano, M. Duchesne, J. Bennett, K.S. Kwong, A. Nakano, R. Hughes,
- 699 Thermodynamic effects of calcium and iron oxides on crystal phase formation in
- synthetic gasifier slags containing from 0 to 27 wt.%  $V_2O_3$ , Fuel, 161 (2015) 364-375.
- 701 https://doi.org/10.1016/j.fuel.2014.11.008.
- 702 [38] S. Seebold, Über den Einfluss der Kristallisation auf das Fließverhalten
- 703 oxidischer Schmelzen, in: Fakultät für Maschinenwesen, Rheinisch-Westfälische
- Technische Hochschule Aachen, Aachen, 2017, pp. 168.
- 705 [39] G. Tammann, W. Hesse, Die Abhängigkeit der Viscosität von der Temperatur bei
- unterkühlten Flüssigkeiten, Zeitschrift für anorganische und allgemeine Chemie, 156
- 707 (1926) 245-257. https://doi.org/10.1002/zaac.19261560121.
- 708 [40] H. Sato, Viscosity measurement of subliquidus magmas:1707 basalt of Fuji
- volcano, Journal of Mineralogical and Petrological Sciences, 100 (2005) 133-142.
- 710 10.2465/jmps.100.133.
- 711 [41] J. Riker, K. Cashman, A. Rust, J. Blundy, Experimental Constraints on
- 712 Plagioclase Crystallization during H 2 O- and H 2 O-CO 2 -Saturated Magma
- Decompression, Journal of Petrology, 56 (2015) 32. 10.1093/petrology/egv059.
- 714 [42] H. Wang, P. Qiu, Y. Li, Z. Han, S. Wu, G. Zhao, Effect of quenching
- 715 temperatures on melting characteristics of coal ash in a reducing atmosphere, Energy
- 716 and Fuels, 26 (2012) 2204-2219. 10.1021/ef300097e.
- 717 [43] F. Vetere, H. Sato, H. Ishibashi, R. De Rosa, P. Donato, Viscosity changes during
- 718 crystallization of a shoshonitic magma: new insights on lava flow emplacement,
- 719 Journal of Mineralogical and Petrological Sciences, 108 (2013) 144-160.
- 720 10.2465/jmps.120724.
- 721 [44] C. He, J. Bai, L. Kong, J. Xu, S. Guhl, X. Li, Z. Ge, X. Cao, Z. Bai, W. Li,
- 722 Effects of atmosphere on the oxidation state of iron and viscosity behavior of coal ash
- 723 slag, Fuel, 243 (2019) 41-51. <a href="https://doi.org/10.1016/j.fuel.2019.01.020">https://doi.org/10.1016/j.fuel.2019.01.020</a>.
- 724 [45] K.V. Cashman, C. Thornber, J.P. Kauahikaua, Cooling and crystallization of lava
- in open channels, and the transition of Pāhoehoe Lava to 'A'ā, Bulletin of
- 726 Volcanology, 61 (1999) 306-323. 10.1007/s004450050299.
- 727 [46] W. Xuan, H. Wang, D. Xia, In-situ observation of crystallization inside coal slags
- 728 and influence of crystals on flow behavior, Fuel, 251 (2019) 242-248.
- 729 https://doi.org/10.1016/j.fuel.2019.04.023.
- 730 [47] V. Goldschmidt, Atlas der Krystallformen, Winter, Heidelberg, 1922.
- 731 [48] G. Tammann, Kristallisieren und Schmelzen: ein Beitrag zur Lehre der
- Änderungen des Aggregatzustandes, Barth, (1903)
- 733 [49] J. Liebertz, Crystal growth from melts of high viscosity, Progress in Crystal
- 734 Growth and Characterization, 6 (1983) 361-369. https://doi.org/10.1016/0146-
- 735 <u>3535(83)90013-8</u>.

740

- 736 [50] G. Wu, E. Yazhenskikh, K. Hack, M. Müller, Viscosity model for oxide melts
- 737 relevant to fuel slags. Part 2: The system SiO2-Al2O3-CaO-MgO-Na2O-K2O, Fuel
- 738 Processing Technology, 138 (2015) 520-533.
- 739 https://doi.org/10.1016/j.fuproc.2015.06.031.